

## Article

# Easily Prepared Transparent Electrodes for Low-Cost Semitransparent Inverted Polymer Solar Cells

Jiaxin Guo, Ziming Bu, Shuo Han, Yanyu Deng, Chunyu Liu \* and Wenbin Guo \*

State Key Laboratory on Integrated Optoelectronics, College of Electronic Science and Engineering, Jilin University, 2699 Qianjin Street, Changchun 130012, China; jxguo19@mails.jlu.edu.cn (J.G.); buzsm20@mails.jlu.edu.cn (Z.B.); hanshuo19@mails.jlu.edu.cn (S.H.); dengyy20@mails.jlu.edu.cn (Y.D.)

\* Correspondence: chunyu\_liu@jlu.edu.cn (C.L.); guowb@jlu.edu.cn (W.G.)

**Abstract:** The continuous thin film of silver (Ag) film is important for semitransparent electrodes in polymer solar cells, while the Ag atoms form as non-continuous below a critical thickness. Here, semitransparent inverted polymer solar cells were fabricated using thermally evaporated Ag/germanium (Ge)/Ag as highly transparent electrodes. An ultra-thin Ge film was introduced to modify the growth mode of Ag. The dependence of the device performance and the thickness of the outer Ag film was investigated. Ag/Ge/Ag electrodes exhibited excellent optical and electrical properties, which were proved by the transmittance and reflectance spectra. A champion efficiency of 5.1% was achieved with an open-circuit voltage level of 0.703 V, a short current density of 11.63 mA/cm<sup>2</sup>, and a fill factor of 63%. The average visible transmittance (300–800 nm) of devices with Ag/Ge/Ag was calculated as 25%.

**Keywords:** polymer solar cells; semitransparent; Ag/Ge/Ag; transmittance; RGB



**Citation:** Guo, J.; Bu, Z.; Han, S.; Deng, Y.; Liu, C.; Guo, W. Easily Prepared Transparent Electrodes for Low-Cost Semitransparent Inverted Polymer Solar Cells. *Energies* **2021**, *14*, 5837. <https://doi.org/10.3390/en14185837>

Academic Editor: I.M. Dharmadasa

Received: 3 August 2021

Accepted: 13 September 2021

Published: 15 September 2021

**Publisher's Note:** MDPI stays neutral with regard to jurisdictional claims in published maps and institutional affiliations.



**Copyright:** © 2021 by the authors. Licensee MDPI, Basel, Switzerland. This article is an open access article distributed under the terms and conditions of the Creative Commons Attribution (CC BY) license (<https://creativecommons.org/licenses/by/4.0/>).

## 1. Introduction

Polymer solar cells (PSCs) show strong competitiveness in future energy sources due to their solution processing, large area printing, easy manufacturing, flexibility, and low material costs [1–13]. In the past decades, the power conversion efficiency (PCE) level has exceeded 18% due to the progress made in bulk heterojunction solar cells [14,15]. Among them, PSCs with semitransparent electrodes show great application prospects [16–21]. An ideal transparent electrode of devices should have both high charge carrier collection efficiency and high transmittance in order to produce better performance. Nevertheless, the poor ability to transport charges—caused by the non-continuous clusters of silver (Ag) atoms of thin-film—results in lower device efficiency, while thicker Ag film causes low transmittance [22]. During the deposition of Ag film, there is a critical thickness of about 15 nm. Ag film deposited on the substrate initially produced isolated islands and formed non-continuous clusters below this thickness. Then, these islands joined together and resulted in a continuous Ag film.

In recent years, a variety of semitransparent electrode structures have been developed [23–25]. Some ultra-thin metal films were introduced to replace Ag in the formation of semitransparent electrodes. For example, a thin gold film was introduced by Li et al. to obtain a single-layer, semitransparent electrode [26]. Despite their excellent transmittance, these solar cell devices suffer from some inherent drawbacks, such as high series resistance and low FF [27–29].

In this paper, a multi-layer electrode structure of Ag/germanium (Ge)/Ag was fabricated and investigated. The growth mode of Ag could be affected by the presence of a germanium (Ge) nucleation layer, which has been reported by Cioarec et al. [30,31]. As reported, Ag atoms were deposited on a Ge layer using a Volmer–Weber model, leading to the small and dense nucleation on dots, which contributed to the fast coalescence (critical

thickness < 1 nm) in the initial step. Eventually, a smooth surface was completed. According to the work in the research of organic light-emitting devices (OLEDs), the ultra-thin Ge layer of 1 nm can also markedly affect the growth mode of Ag [32]. The potential of the Ag/Ge/Ag electrode was further explored in the PSCs. The dependence of device performance on the thickness of each layer was investigated; meanwhile, the transmittance, reflectance, and color-neutrality of the different electrodes are also analyzed through various thicknesses of the Ag capping layer.

## 2. Experimental

The photovoltaic device has the structure of ITO/polyethyleneimine (PEI)/PTB7:PC<sub>71</sub>BM/MoO<sub>3</sub>/Ag/Ge/Ag, as shown schematically in Figure 1. The electron acceptor material of PC<sub>71</sub>BM and the electron donor material of PTB7 were obtained from 1-Material Inc. (Hackensack, NJ, USA) and Lumtek Corp., respectively, without any purification. To fabricate inverted PSCs, ITO-coated substrates were precleaned using acetone, ethanol, and de-ionized water, respectively, and were then dried using nitrogen. Subsequently, PEI was dissolved in deionized water at a concentration of 1 mg/mL and spin-casted on the ITO substrate to produce ETL. Afterward, PEI films were thermally annealed at 100 °C for 15 min. PTB7 was dissolved in chlorobenzene to produce a 10 mg/mL solution, followed by blending with PC<sub>71</sub>BM in a 2:3 weight ratio. The blend was stirred for 72 h before spin-coating on the top of PEI film and was then dried for 3–5 min in the air. Finally, the devices were transferred into a vacuum chamber. The MoO<sub>3</sub> buffer layer (8 nm) and the Ag/Ge/Ag electrode layer, with different thickness compositions, were thermally evaporated in sequence under a high vacuum ( $\sim 10^{-5}$  Tor) without disrupting the vacuum [33]. The evaporation rate of Ag (1 nm)/Ge (1 nm) deposition was 0.02 Å/s. Finally, the coater Ag film was deposited with an evaporation rate of 0.20 Å/s.

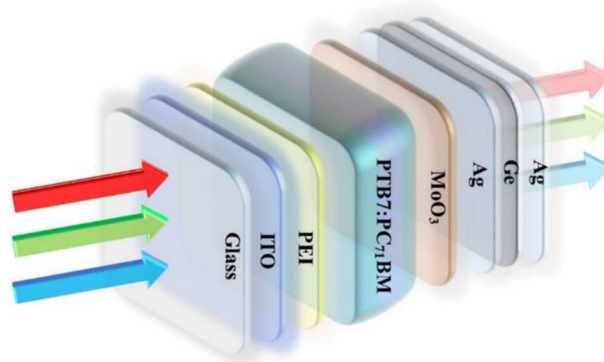


**Figure 1.** Structure diagram of PSCs with the Ag/Ge/Ag semitransparent electrode.

The Ag/Ge/Ag electrode area of the device is defined by the shadow mask. The current density–voltage ( $J$ - $V$ ) characteristics were measured using a computer-programmed Keithley 2400 source/meter under Air Mass 1.5 Global (AM 1.5 G) solar illuminations with an Oriel 300 W solar simulator intensity of  $100 \text{ mW cm}^{-2}$  [34]. The light intensity was calibrated with a photometer (International light, IL1400), which was corrected using a standard silicon solar cell. The incident photon-to-current efficiency (IPCE) spectra of devices were also measured. The transmission and reflection spectra were measured using an ultra-violet/visible spectrometer (UV 1700, Shimadzu, Kyoto, Japan). The morphology of Ag films was investigated through scanning electron microscopy (SEM) using an LEO 1525 Gemini high-resolution field emission gun scanning electron microscope. The work function (WF) of the Ag/Ge/Ag film was calculated through ultraviolet photoelectron spectra (UPS) measurement using He I radiation. The morphology of the electrode was tested through atomic force microscopy (AFM) in the tapping mode (Dimension Icon Scanasyt). The color perception indices were calculated using the CIE 1931 xy color

space to quantify the color-neutrality of different films. All average parameters of device performance in this study were summarized for over 32 devices.

### 3. Result and Discussion

To investigate the role of the Ag/Ge/Ag electrode on the performance of PSCs, the devices with Ag (1 nm)/Ge (1 nm)/Ag (10, 12, 14, and 16 nm) and single Ag layers (15 nm) were fabricated and tested. The thickness of a single Ag electrode was decided using the critical thinness, below which the Ag atoms form non-continuous clusters [32]. The  $J$ - $V$  characteristics of devices, illuminated from the ITO side and Ag/Ge/Ag side, are shown in Figure 2a,b. A summary of the average parameters of the device performance is shown in Table 1. With a  $J_{SC}$  of 10.07 mA/cm<sup>2</sup>, a  $V_{OC}$  of 0.673 V, and an FF of 56%, a device with a single Ag electrode yields a lower PCE of 3.8%. Conversely, a significant increase in  $J_{SC}$  is observed in devices with the Ag/Ge/Ag electrode. When the thickness of the Ag capping layer was 14 nm—possessing the same Ag thickness as with a single Ag electrode—the performance of the device was dramatically enhanced, indicating that the conductivity and hole collection abilities of the Ag/Ge/Ag electrode were improved through the incorporation of 1 nm Ge. The composite Ag/Ge/Ag electrode influenced the growth mode of the Ag through the growth of denser and smaller nucleation in the initial step, which lead to a more continuous and smoother surface. Thus, the performance of PSCs was significantly increased. However, even the ultra-thin Ge film can influence the growth mode of Ag; devices with an Ag capping layer of less than 14 nm still exhibited poor performance. Moreover, the devices with a thicker Ag capping layer of 16 nm were fabricated and measured; the results showed a PCE of 5.1%, which indicates no enhancement when compared with the device with a 14 nm Ag capping layer. Besides, the transmittance of the semitransparent electrode would be affected by a thicker Ag film of 16 nm. Therefore, the Ag/Ge/Ag (14 nm) was supposed to be the optimal semitransparent structure. The  $J$ - $V$  characteristics in the forward and reverse scans were also measured and are shown in Figure S1. The parameters are listed in Table S1. The statistical data for 32 devices, as well as the stability of the devices stored in the air, are shown in Figure 2e,f. An enhancement in stability was observed for devices with the Ag/Ge/Ag electrode, which could be attributed to the denser morphology of the upper coated electrode.

**Table 1.** Characteristic data of semitransparent inverted PSCs with different thicknesses of the Ag capping layer, as illuminated from the ITO (bottom) and the Ag/Ge/Ag (top) sides.

Device (nm)	Illumination	$J_{SC}$ (mA/cm <sup>2</sup> )	$V_{OC}$ (V)	FF (%)	PCE (%)
Single Ag 15	Bottom	10.07	0.673	56	3.8
Single Ag 15	Top	1.96	0.626	58	0.7
Ag/Ge/Ag 10	Bottom	10.16	0.688	62	4.3
Ag/Ge/Ag 10	Top	2.39	0.651	62	1.0
Ag/Ge/Ag 12	Bottom	11.18	0.686	61	4.7
Ag/Ge/Ag 12	Top	2.51	0.654	61	1.0
Ag/Ge/Ag 14	Bottom	11.63	0.703	63	5.1
Ag/Ge/Ag 14	Top	2.27	0.659	66	1.0
Ag/Ge/Ag 16	Bottom	11.75	0.702	62	5.1
Ag/Ge/Ag 16	Top	2.04	0.660	69	1.0

When the light was illuminated from the top side, the absorption of the active layer material was directly proportional to the transmittance of the incidence electrode, which means the thinnest Ag layer would result in the largest absorption. However, the device with a 10 nm Ag layer exhibited a lower  $J_{SC}$  compared to the device with a 12 nm Ag layer. This decrease was attributed to the non-continuous clusters, which had not formed a smooth surface. Moreover, the unsmooth  $J$ - $V$  curve of the device also confirmed the unstable transport ability and unequal illumination caused by the non-continuous clusters of the 10 nm Ag layer [35,36], which was consist with the lower  $J_{SC}$ . With the increase in the Ag capping layer from 12 nm to 16 nm, the  $J_{SC}$  value gradually decreased due to the lower

transmittance. It can be seen that the  $V_{OC}$  of devices from the top illumination measurement was significantly decreased. The dependence of the  $V_{OC}$  and the photo-current ( $I_{ph}$ ) can be generally expressed as follows [37]:

$$V_{OC} = \frac{KT}{q} \log\left(\frac{I_{ph}}{I_s} + 1\right) \quad (1)$$

where  $I_s$  is the reverse saturation current,  $K$  is the Boltzman constant,  $T$  is the temperature, and  $q$  is the charge. In Equation (1),  $V_{OC}$  is directly proportional to  $I_{ph}$ . The  $I_{ph}$  from the ITO side was much bigger than that from the Ag/Ge/Ag side, which is shown in Table 1.

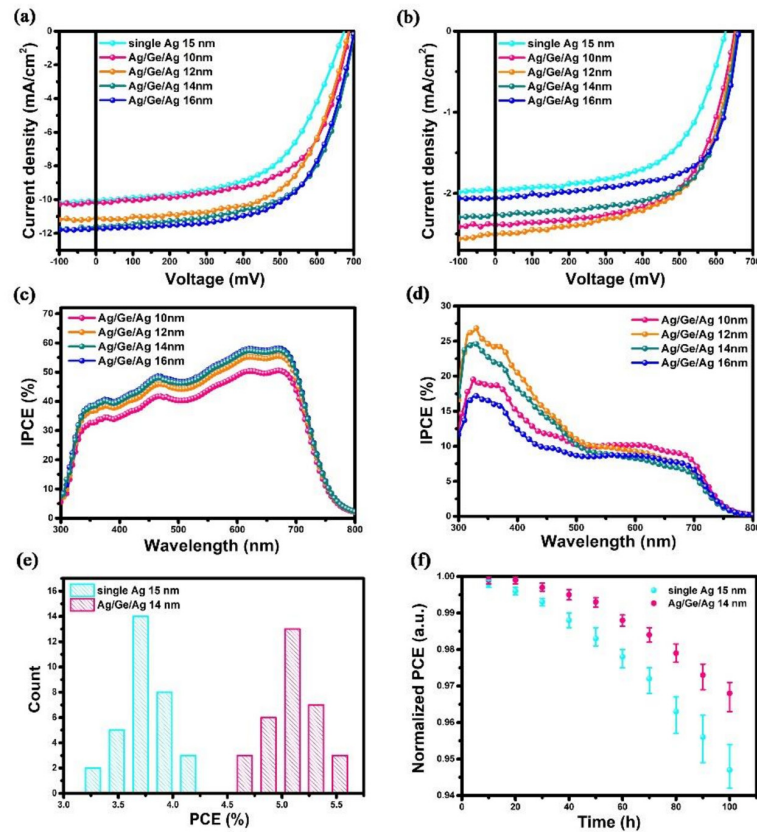


**Figure 2.**  $J$ - $V$  characteristics of devices with a single Ag electrode (15 nm) and ITO/PEI/PTB7:PC<sub>71</sub>BM/MoO<sub>3</sub>/Ag (1 nm)/Ge (1 nm)/Ag (10, 12, 14, and 16 nm) depending on the thickness of the Ag capping layer when illuminated from (a) the ITO side and (b) the Ag/Ge/Ag side. IPCE spectra of devices measured from (c) the ITO side and (d) the Ag/Ge/Ag side. (e) The histograms for the performance of devices with a single Ag electrode and Ag/Ge/Ag electrode. (f) The normalized PCE of devices with a single Ag electrode and a Ag/Ge/Ag electrode.

To further explore the relationship between the  $J_{SC}$  value and electrode thickness, the IPCE values of the devices were measured when the light was illuminated from both the ITO side (Figure 2c) and the Ag/Ge/Ag electrode side (Figure 2d). As shown in Figure 2c, with the Ag capping layer increased from 10 nm to 16 nm, the IPCE was enhanced in the whole range from 300 nm to 800 nm. The enhancement was attributed to the improved conductivity of the continuous Ag film and the increased reflected light. As for the IPCE measured from the Ag/Ge/Ag electrode side, the value did not decrease linearly with the Ag thickness. The highest IPCE was not observed from the device with the Ag/Ge/Ag (10 nm) electrode, which achieved the highest transmittance value and allowed more incident light to the active layer. The highest IPCE value of 26.85% was observed at 330 nm from the device with the Ag/Ge/Ag (12 nm) electrode due to its better continuity compared to 10 nm Ag.

In order to explore the uniformity of evaporated Ag and Ge, the SEM-EDX images of Ag (1 nm)/Ge (1 nm) and Ag (1 nm)/Ge (1 nm)/Ag (14 nm) were measured and are shown in Figure 3a,b. The composition of Ag is represented by the color red and the composition of Ge is represented by the color green. The mass fraction of Ge is 26.06% and Ag is 73.94% for the Ag/Ge film with uniform separation of Ag and Ge. In the Ag/Ge/Ag layer, the composition of Ag became continuous. The mass fraction of Ge is 1.87% and Ag is 98.13%. According to a study of Ag/Ge deposition, the film of the semitransparent electrode becomes more compact with the incorporation of Ge [38–42]. The WF of the Ag/Ge/Ag layer, calculated through UPS, was  $-4.18$  eV (Figure S2). In order to further understand the role of Ge on the Ag deposition, the morphology of the Ag film was examined using SEM. Figure 3c,d displays Ag film deposited on MoO<sub>3</sub>, with thicknesses of 3 nm and 12 nm, while Figure 3e,f displays Ag film deposited on Ag (1 nm)/Ge (1 nm) film, with thicknesses of 3 nm and 12 nm. When the thickness of the Ag film on MoO<sub>3</sub> was 3 nm, the Ag islands with larger sizes can be clearly seen when compared with Ag deposited on the Ag/Ge film. The Ag islands deposited on the Ag/Ge film exhibited better morphology, as they were much smaller and denser. Finally, Ag deposited on MoO<sub>3</sub> formed a film with obvious gaps, which will affect the conductivity of the Ag electrode [43], while Ag deposited on the Ag/Ge film exhibited a film with a smoother surface where gaps can barely be seen. To further elucidate the growth mode of Ag, Figure 4 shows that morphology is altered with the Ag deposited on the MoO<sub>3</sub> (Figure 4a,b) and Ag/Ge (Figure 4c,d) films. When Ag atoms were deposited directly on MoO<sub>3</sub>, the clusters were formed with larger sizes and larger gaps (Figure 4a). The merging of clusters was difficult due to the gaps. Finally, the gaps affected the performance of the semitransparent electrode (Figure 4b). However, Ag atoms deposited on an Ag/Ge film grew in the Volmer–Weber model due to the larger activation energy for Ag diffusion on a Ge surface, leading to smaller and denser nucleation on dots in the initial step (Figure 4c) [39]. As a consequence, the fast coalescence was completed with small clusters within a thickness of 1 nm. With clusters growing and merging during the thermal depositing, a uniform and dense film with the optimized electrical property was eventually formed (Figure 4d). AFM images of the single Ag film and the Ag/Ge/Ag film were also measured (Figure 4e,f). It can be seen that the size of the clusters on the surface of the Ag/Ge/Ag film was significantly decreased compared to the clusters on the single Ag surface. The roughness of the single Ag film is 1.31 nm, while the roughness of the Ag/Ge/Ag film is 0.69 nm.

To further elucidate the properties of semitransparent electrodes, the reflectance and transmittance spectra of the Ag (1 nm)/Ge (1 nm)/Ag (10, 12, 14, and 16 nm) films were measured. The reflectance spectra from 320 nm to 800 nm were measured and are shown in Figure 5a. Further, the absorption spectrum of the active layer was included to make a comparison. The reflectance was enhanced with the increase in the wavelength, which matches the absorption spectrum of the active layer in the range 450–700 nm, so that the  $J_{SC}$  was increased with the deposition of Ag when illuminated from the ITO side. The photo in Figure 5b displays a printed school emblem of a university covered by a 100 nm Ag film (left) and an Ag/Ge/Ag (14 nm) film. The logo is clearly observed through the Ag/Ge/Ag film, while the logo under the Ag film is invisible. The sight of the building through the Ag/Ge/Ag film under natural light is also shown in this inset picture. The reflectance, transmittance, and absorbance spectra of the Ag (15 nm) and the Ag/Ge/Ag (14 nm) films were plotted separately in Figure S3. The optical transmittance spectrum of the semitransparent device with the Ag/Ge/Ag electrode is shown in Figure 5c. Further, the RGB picture observed through the device with the Ag/Ge/Ag electrode (right) is still clear and vivid compared to the origin RGB picture (left). The ATV of devices with Ag/Ge/Ag was calculated as 25%, which is generally agreed to be the benchmark for window applications [44]. To quantify the color-neutrality of devices with the semitransparent electrode, color perception indices of the device with the Ag/Ge/Ag semitransparent electrode were calculated and are displayed in the CIE 1931 xy chromaticity diagram in Figure 5d. Meanwhile, AM1.5 illumination is also shown in the diagram.

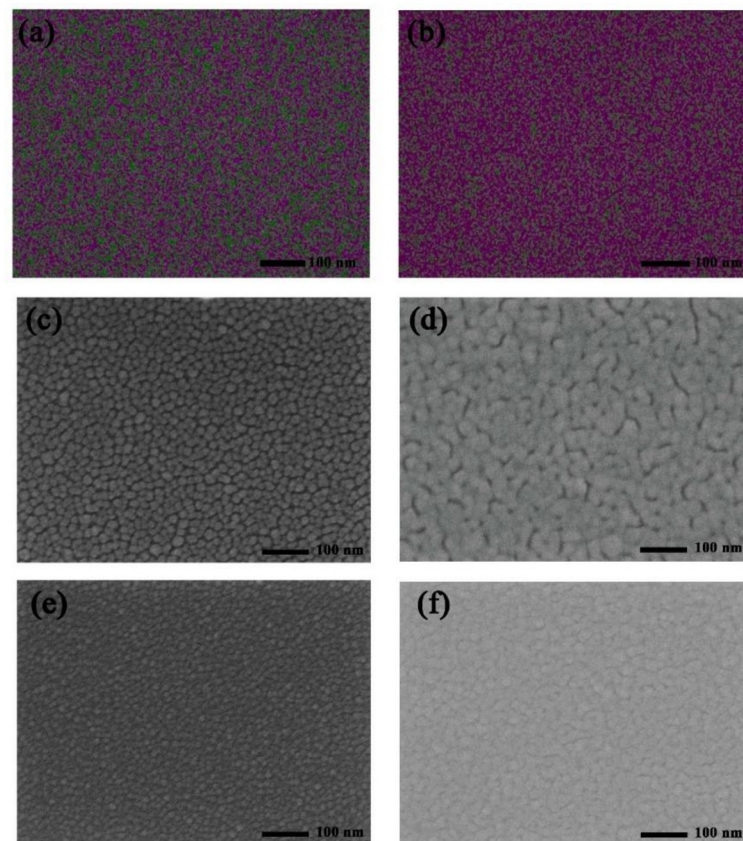


**Figure 3.** Elemental mapping of the elements Ag (red), Ge (green) in (a) the Ag/Ge film and (b) the Ag/Ge/Ag film. SEM images of the Ag films with structures of (c) MoO<sub>3</sub>/Ag (3 nm), (d) MoO<sub>3</sub>/Ag (12 nm), (e) Ag/Ge/Ag (3 nm), and (f) Ag/Ge/Ag (12 nm).

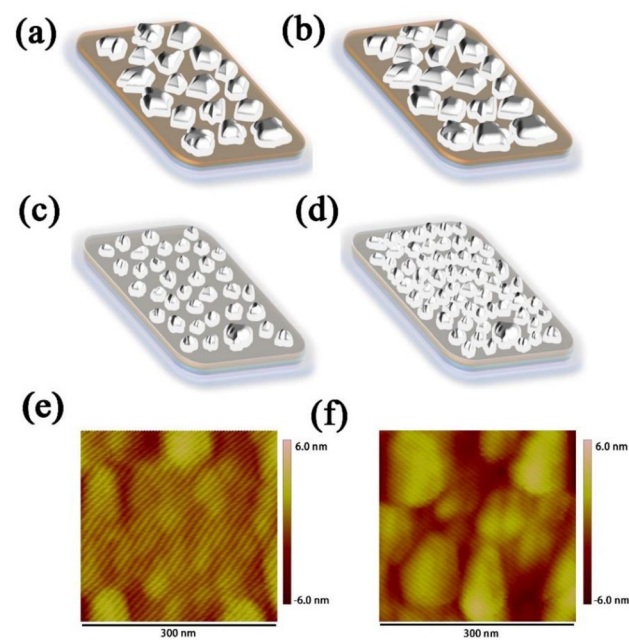


**Figure 4.** Schematic of the ultra-thin Ag film morphology changing with the increase in film thickness on (a,b) the MoO<sub>3</sub> film and (c,d) the Ag/Ge film. AFM images of (e) the Ag/Ge/Ag film and (f) the single Ag film.

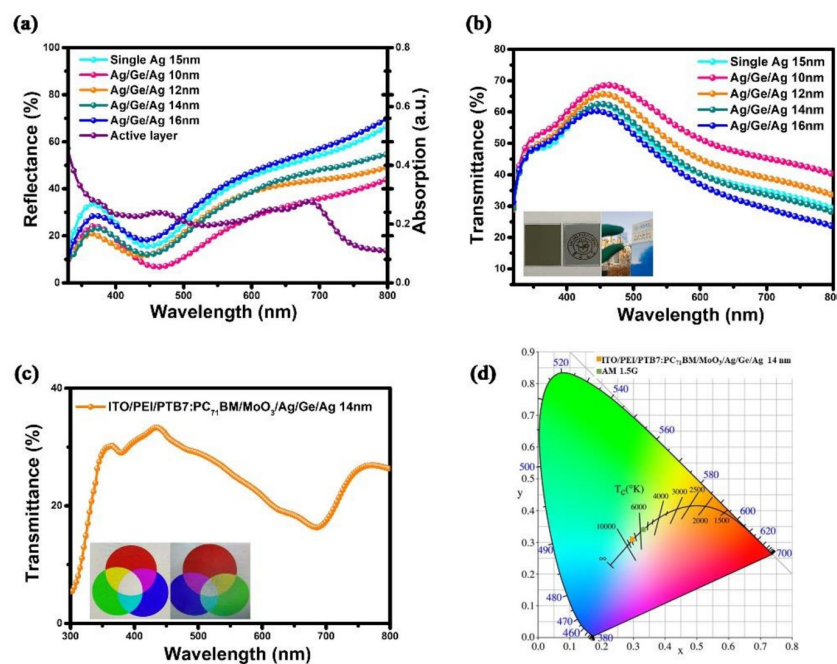


**Figure 5.** (a) Reflectance spectra and (b) transmittance spectra of the semitransparent electrode Ag/Ge/Ag (10, 12, 14, and 16 nm). (c) Transmittance spectrum of the semitransparent device with the Ag/Ge/Ag (14 nm) electrode. (d) Color coordinates of devices on the CIE xy 1931 chromaticity diagram.

#### 4. Conclusions

In summary, we present efficient semitransparent inverted PSCs comprising an Ag/Ge/Ag multilayer structure as the transparent electrode. The ultra-thin Ge layer was introduced to affect the Ag growth mode, contributing to the fast coalescence (critical thickness <1 nm) in the initial step. Eventually, a smoother surface of Ag was fabricated, which is more efficient than a single semitransparent Ag electrode. The performance of devices with different thicknesses of each layer was investigated, and a PCE of 5.1% was achieved when the structure of the electrode was Ag (1 nm)/Ge (1 nm)/Ag (14 nm) with an AVT of 25%.

**Supplementary Materials:** The following are available online at <https://www.mdpi.com/article/10.3390/en14185837/s1>, Figure S1: (a) *J-V* characteristics in forward and reverse scans of the device with a single Ag electrode and (b) device with Ag/Ge/Ag 14 nm electrode; Table S1: *J-V* Parameters of devices with single Ag and Ag/Ge/Ag electrode in forward and reverse scan direction; Figure S2: UPS spectrum of Ag/Ge/Ag film; Figure S3: (a) The reflectance, absorbance and transmittance curves of single Ag 15 nm and (b) Ag/Ge/Ag 14 nm.

**Author Contributions:** J.G. preparation and measurement. Z.B.; validation, J.G. and S.H.; formal analysis, Y.D.; investigation, J.G. and C.L.; writing—original draft preparation and writing—review and editing, W.G.; supervision. All authors have read and agreed to the published version of the manuscript.

**Funding:** This research received no external funding.

**Data Availability Statement:** The data that support the findings of this study are available from the corresponding authors upon reasonable request.

**Acknowledgments:** The authors are grateful to the National Natural Science Foundation of China (62175084,62005093), the Scientific Research Planning Project of the Education Department of Jilin Province (JJKH20200980KJ), and the Industrial Technology Research and Development Project of Jilin Province (2020C026-5) for the support of this work.

**Conflicts of Interest:** The authors declare no conflict of interest.

## References

1. Dennler, G.; Scharber, M.C.; Brabec, C.J. Polymer-fullerene bulk-heterojunction solar cells. *Adv. Mater.* **2009**, *21*, 1323–1338. [[CrossRef](#)]
2. Chen, X.; Jia, B.H.; Zhang, Y.A.; Gu, M. Exceeding the Limit of Plasmonic Light Trapping in Textured Screen-printed Solar Cells Using Al Nanoparticles and Wrinkle-like Graphene Sheets. *Light Sci. Appl.* **2013**, *2*, e92. [[CrossRef](#)]
3. Tang, C.W. Two-layer organic photovoltaic cell. *Appl. Phys. Lett.* **1986**, *48*, 183–185. [[CrossRef](#)]
4. Li, X.C.; Xie, F.X.; Zhang, S.Q.; Hou, J.H.; Choy, W.C. MoO<sub>x</sub> and V<sub>2</sub>O<sub>5</sub> as Hole and Electron Transport Layers Through Functionalized Intercalation in Normal and Inverted Organic Optoelectronic Devices. *Light Sci. Appl.* **2015**, *4*, e273. [[CrossRef](#)]
5. Zhang, Y.; Zhou, H.; Seifert, J.; Ying, L.; Mikhailovsky, A.; Heeger, A.J.; Bazan, G.C.; Nguyen, T.Q. Molecular Doping Enhances Photoconductivity in Polymer Bulk Heterojunction Solar Cells. *Adv. Mater.* **2013**, *25*, 7038–7044. [[CrossRef](#)] [[PubMed](#)]
6. Guo, C.F.; Sun, T.S.; Cao, F.; Liu, Q.; Ren, Z. Metallic Nanostructures for Light Trapping in Energy-harvesting Devices. *Light Sci. Appl.* **2014**, *3*, e161.
7. Park, B.; Yun, S.H.; Cho, C.Y.; Kim, Y.C.; Shin, J.C.; Jeon, H.G.; Huh, Y.H.; Hwang, I.; Baik, K.Y.; Lee, Y.I.; et al. Surface plasmon excitation in semitransparent inverted polymer photovoltaic devices and their applications as label-free optical sensors. *Light Sci. Appl.* **2014**, *3*, e222. [[CrossRef](#)]
8. Lee, K.; Lee, J.; Mazor, B.A.; Forrest, S.R. Transforming the cost of solar-to-electrical energy conversion: Integrating thin-film GaAs solar cells with non-tracking mini-concentrators. *Light Sci. Appl.* **2015**, *4*, e288. [[CrossRef](#)]
9. Zhong, Y.; Trinh, M.T.; Chen, R.; Purdum, G.E.; Khlyabich, P.P.; Sezen, M.; Oh, S.; Zhu, H.; Fowler, B.; Zhang, B.; et al. Molecular helices as electron acceptors in high-performance bulk heterojunction solar cells. *Nat. Commun.* **2015**, *6*, 1–8. [[CrossRef](#)] [[PubMed](#)]
10. Su, Y.H.; Ke, Y.F.; Cai, S.L.; Yao, Q.Y. Surface Resonance of Layer-by-Layer Gold Nanoparticles Induced Photoelectric Current in Environmentally-friendly Plasmon-Sensitized Solar Cell. *Light Sci. Appl.* **2012**, *1*, e14. [[CrossRef](#)]
11. Blum, O.; Shaked, N.T. Predication of photothermal phase signatures from arbitrary plasmonic nanoparticles and experimental verification. *Light Sci. Appl.* **2015**, *4*, e322. [[CrossRef](#)]
12. Kosten, E.D.; Atwater, J.H.; Parsons, J.; Polman, A.H.; Atwater, A. Highly Efficient GaAs Solar Cells by Limiting Light Emission Angle. *Light Sci. Appl.* **2013**, *2*, e45. [[CrossRef](#)]
13. Huang, W.; Cheng, P.; Yang, Y.; Li, G.; Yang, Y. High-Performance Organic Bulk-Heterojunction Solar Cells Based on Multiple-Donor or Multiple-Acceptor Components. *Adv. Mater.* **2018**, *30*, 1705706. [[CrossRef](#)] [[PubMed](#)]
14. Chen, H.-Y.; Hou, J.; Zhang, S.; Liang, Y.; Yang, G.; Yang, Y.; Yu, L.; Wu, Y.; Li, G. Polymer solar cells with enhanced open-circuit voltage and efficiency. *Nat. Photonics* **2009**, *3*, 649–653. [[CrossRef](#)]
15. Deibel, C.; Dyakonov, V. Polymer-fullerene bulk heterojunction solar cells. *Rep. Prog. Phys.* **2010**, *73*, 096401. [[CrossRef](#)]
16. Gilot, J.; Wienk, M.M.; Janssen, R.A.J. Optimizing Polymer Tandem Solar Cells. *Adv. Mater.* **2010**, *22*, E67–E71. [[CrossRef](#)] [[PubMed](#)]
17. Hu, Z.H.; Wang, J.; Ma, X.L.; Gao, J.H.; Xu, C.Y.; Wang, X.L.; Zhang, X.L.; Wang, Z.; Zhang, F.J. Semitransparent organic solar cells exhibiting 13.02% efficiency and 20.2% average visible transmittance. *J. Mater. Chem. A* **2021**, *9*, 6797–6804. [[CrossRef](#)]
18. Hu, Z.H.; Wang, Z.; An, Q.S.; Zhang, F.J. Semitransparent polymer solar cells with 12.37% efficiency and 18.6% average visible transmittance. *Sci. Bull.* **2020**, *65*, 131–137. [[CrossRef](#)]
19. Hu, Z.H.; Wang, J.; Ma, X.L.; Gao, J.H.; Xu, C.Y.; Yang, K.X.; Wang, Z.; Zhang, J.; Zhang, F.J. A critical review on semitransparent organic solar cells. *Nano Energy* **2020**, *78*, 105376. [[CrossRef](#)]
20. Sista, S.; Park, M.-H.; Hong, Z.; Wu, Y.; Hou, J.; Kwan, W.L.; Li, G.; Yang, Y. Highly efficient tandem polymer photovoltaic cells. *Adv. Mater.* **2010**, *22*, 380–383. [[CrossRef](#)] [[PubMed](#)]
21. Chung, W.-S.; Lee, H.; Lee, W.; Ko, M.J.; Park, N.-G.; Ju, B.-K.; Kim, K. Solution processed polymer tandem cell utilizing organic layer coated nano-crystalline TiO<sub>2</sub> as interlayer. *Org. Electron.* **2010**, *11*, 521–528. [[CrossRef](#)]
22. Van De Groep, J.; Spinelli, P.; Polman, A. Transparent conducting silver nanowire networks. *Nano Lett.* **2012**, *12*, 3138–3144. [[CrossRef](#)] [[PubMed](#)]
23. Li, G.; Chu, C.-W.; Shrotriya, V.; Huang, J.; Yang, Y. Efficient inverted polymer solar cells. *Appl. Phys. Lett.* **2006**, *88*, 253503. [[CrossRef](#)]
24. Ng, G.-M.; Kietzke, E.L.; Kietzke, T.; Tan, L.-W.; Liew, P.-K.; Zhu, F. Optical enhancement in semitransparent polymer photovoltaic cells. *Appl. Phys. Lett.* **2007**, *90*, 103505. [[CrossRef](#)]
25. Chen, F.-C.; Wu, J.-L.; Hsieh, K.-H.; Chen, W.-C.; Lee, S.-W. Polymer photovoltaic devices with highly transparent cathodes. *Org. Electron.* **2008**, *9*, 1132–1135. [[CrossRef](#)]
26. Huang, J.; Li, G.; Yang, Y. A semi-transparent plastic solar cell fabricated by a lamination process. *Adv. Mater.* **2008**, *20*, 415–419. [[CrossRef](#)]
27. Yim, J.H.; Joe, S.-Y.; Pang, C.; Lee, K.M.; Jeong, H.; Park, J.-Y.; Ahn, Y.H.; de Mello, J.C.; Lee, S. Fully solution-processed semitransparent organic solar cells with a silver nanowire cathode and a conducting polymer anode. *ACS Nano* **2014**, *8*, 2857–2863. [[CrossRef](#)]
28. Yu, W.; Jia, X.; Long, Y.; Shen, L.; Liu, Y.; Guo, W.; Ruan, S. Highly efficient semitransparent polymer solar cells with color rendering index approaching 100 using one-dimensional photonic crystal. *ACS Appl. Mater. Interfaces* **2015**, *7*, 9920–9928. [[CrossRef](#)]

29. Chen, C.-C.; Dou, L.; Zhu, R.; Chung, C.-H.; Song, T.-B.; Zheng, Y.B.; Hawks, S.; Li, G.; Weiss, P.S.; Yang, Y. Visibly transparent polymer solar cells produced by solution processing. *ACS Nano* **2012**, *6*, 7185–7190. [[CrossRef](#)]
30. Cioarec, C.; Melpignano, P.; Gherardi, N.; Clergereaux, R.; Villeneuve, C. Ultrasooth silver thin film electrodes with high polar liquid wettability for OLED microcavity application. *Langmuir* **2011**, *27*, 3611–3617. [[CrossRef](#)]
31. Melpignano, P.; Cioarec, C.; Clergereaux, R.; Gherardi, N.; Villeneuve, C.; Datas, L. E-beam deposited ultra-smooth silver thin film on glass with different nucleation layers: An optimization study for OLED micro-cavity application. *Org. Electron.* **2010**, *11*, 1111–1119. [[CrossRef](#)]
32. Liu, S.; Liu, W.; Yu, J.; Zhang, W.; Zhang, L.; Wen, X.; Yin, Y.; Xie, W. Silver/germanium/silver: An effective transparent electrode for flexible organic light-emitting devices. *J. Mater. Chem. C* **2014**, *2*, 835–840. [[CrossRef](#)]
33. Xia, R.; Brabec, C.J.; Yip, H.-L.; Cao, Y. High-throughput optical screening for efficient semitransparent organic solar cells. *Joule* **2019**, *3*, 2241–2254. [[CrossRef](#)]
34. Li, Z.; Zhang, X.; Liu, C.; Zhang, Z.; He, Y.; Li, J.; Shen, L.; Guo, W.; Ruan, S. The performance enhancement of polymer solar cells by introducing cadmium-free quantum dots. *J. Phys. Chem. C* **2015**, *119*, 26747–26752. [[CrossRef](#)]
35. Kang, T.S.; Chun, K.H.; Hong, J.S.; Moon, S.H.; Kim, K.J. Enhanced stability of photocurrent-voltage curves in Ru (II)-dye-sensitized nanocrystalline TiO<sub>2</sub> electrodes with carboxylic acids. *J. Electrochem. Soc.* **2000**, *147*, 3049. [[CrossRef](#)]
36. Ahmed, R.T. Obtaining and analyzing the characteristics curves of a solar cell. *IJOCAAS* **2017**, *2*, 94–98. [[CrossRef](#)]
37. Moliton, A.; Nunzi, J.-M. How to model the behaviour of organic photovoltaic cells. *Polym. Int.* **2006**, *55*, 583–600. [[CrossRef](#)]
38. Bahmani, E.; Zakeri, A.; Aghdam, A. Microstructural analysis and surface studies on Ag-Ge alloy coatings prepared by electrodeposition technique. *J. Mater. Sci.* **2021**, *56*, 6427–6447. [[CrossRef](#)]
39. Brenner, A. *Electrodeposition of Alloys: Principles and Practice*; Elsevier: Amsterdam, The Netherlands, 2013.
40. Kumaraguru, S.; Pavulraj, R.; Vijayakumar, J.; Mohan, S. Electrodeposition of cobalt/silver multilayers from deep eutectic solvent and their giant magnetoresistance. *J. Alloy. Compd.* **2017**, *693*, 1143–1149. [[CrossRef](#)]
41. Łukaszewski, M.; Klimek, K.; Czerwiński, A. Microscopic, spectroscopic and electrochemical characterization of the surface of Pd–Ag alloys. *J. Electroanal. Chem.* **2009**, *637*, 13–20. [[CrossRef](#)]
42. Tai, C.; Su, F.; Sun, I. Electrodeposition of palladium–silver in a Lewis basic 1-ethyl-3-methylimidazolium chloride-tetrafluoroborate ionic liquid. *Electrochim. Acta* **2005**, *50*, 5504–5509. [[CrossRef](#)]
43. Sun, G.; Shahid, M.; Fei, Z.; Xu, S.; Eisner, F.D.; Anthopolous, T.D.; McLachlan, M.A.; Heeney, M. Highly-efficient semi-transparent organic solar cells utilizing non-fullerene acceptors with optimized multilayer MoO<sub>3</sub>/Ag/MoO<sub>3</sub> electrodes. *Mater. Chem. Front.* **2019**, *3*, 450–455. [[CrossRef](#)]
44. Xu, G.; Shen, L.; Cui, C.; Wen, S.; Xue, R.; Chen, W.; Chen, H.; Zhang, J.; Li, H.; Li, Y.; et al. High performance colorful semitransparent polymer solar cells with ultrathin hybrid-metal electrodes and fine-tuned dielectric mirrors. *Adv. Funct. Mater.* **2017**, *27*, 1605908. [[CrossRef](#)]